Impinging Jets Confined by a Conical Wall: Laminar Flow Predictions

João M. Miranda and João B. L. M. Campos
Centro de Estudos de Fenómenos de Transporte, Dept. de Engenharia Química,
Faculdade de Engenharia da Universidade do Porto, 4099 Porto Codex, Portugal

A laminar jet flow confined by a conical wall and an impinging plate was investigated. The Navier-Stokes equations were numerically solved by a finite difference technique and the results compared with laser Doppler anemometry data, the latter also covering the transition and turbulent flow regimes. Transition was found to start in the impingement region at a jet Reynolds number of around 1,600. The investigation concentrated on assessing the effects of nozzle-to-plate distance (always less than one nozzle diameter), jet Reynolds number, and nozzle outlet conditions. The shape of the velocity profile at the nozzle outlet determines the entire cell flow field, whereas nozzle-to-plate distance affects the flow in the expansion region. Under certain flow and geometric conditions a recirculation zone appears in the expansion region, in the vicinity of the plate.

Introduction

Impinging jets are encountered in many industrial applications, such as in paper and textile drying processes, in steel mills, glass tempering, turbine blades, and electronic components cooling. The jet impinges on a solid surface and spreads out along the surface with a high radial velocity, thus inducing high mass- and heat-transfer rates.

Two types of liquid single-phase jets are commonly referred to in the literature: submerged jets and free-surface jets. In submerged jets the liquid jet issues into a region containing the same liquid at rest, whereas in free-surface jets the liquid jet is surrounded by ambient air (by a gas). Submerged jets can be unconfined or confined by an upper surface, usually by a plate attached to the nozzle and parallel to the impingement surface. This article describes the investigation of a laminar impinging jet, confined by a conical wall extended from the nozzle to a short distance above the impingement plate (0.1 to 0.3 nozzle diameters).

Garimella and Rice (1995) divided the flow field of an impinging jet into three regions: the free-jet region, the impingement region, and the wall region. The flow in the free-jet region is axial and is not affected by the presence of the impingement plate; at the nozzle exit, the axial velocity starts to decay and the jet spreads to the surroundings. Gardon and Akfirat (1965) and Martin (1977) have shown that the flow of turbulent jets starts to be affected by the impingement surface at approximately 1.2 nozzle diameters from this surface. In the present laminar study, the nozzle-to-plate distance is lower than 1.0 nozzle diameter and, as will be shown later, the effect of the surface starts near the nozzle exit. At the impingement region, the fluid accelerates and is forced to change to the radial direction. At the wall region, the flow is predominantly radial with a growing boundary layer.

In a coming article, results of experimental and numerical studies on mass transfer from a soluble impingement plate will be presented. The emphasis in the present article is to investigate the flow hydrodynamics and the effects of several geometric and dynamic parameters and to select one configuration for the mass-transfer experiments. The final objective of such studies is to simulate and investigate the flow and the mass-transfer rates near a separation membrane, in particular to investigate the so-called polarization effect.

The numerical methods employed to solve the Navier-Stokes equations are described in the next section. It follows the description of the experimental setup and of the laser Doppler technique. After that, the numerical predictions are interpreted and compared with the experimental data.

Correspondence concerning this article should be addressed to J. B. L. M. Campos.

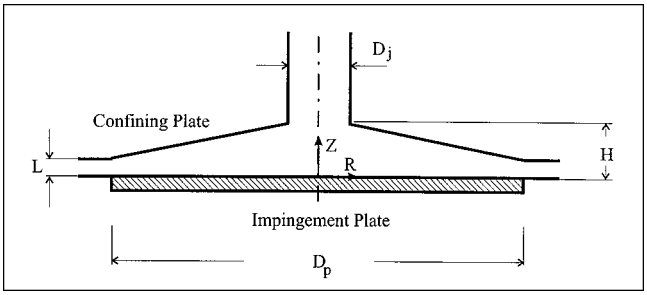

Figure 1. The cell.

Numerical Studies

The objective of the numerical study is to predict the laminar flow pattern inside the conical cell. To this purpose, there were two possibilities: either integrate numerically the proper flow equations or use a commercial CFD code. The second option was straightforward, but the development of a new code to study mass transfer near a separation membrane (reverse osmoses and ultrafiltration processes) was preferred for this investigation.

Polat et al. (1989) reviewed the numerical literature on flow and heat-transfer characteristics of impinging jets. They reviewed the numerical studies on unconfined and confined (by a plane wall) impinging jets in both the laminar and turbulent regimes, and summarized the corresponding numerical techniques. The effects of physical and geometric parameters on flow patterns and on heat-transfer rates were also described.

Various numerical predictions of impinging jet flows have been carried out, most of them referring to turbulent regime. Miyazaki and Silberman (1972) studied the flow and heat-transfer characteristics of a two-dimensional laminar unconfined impinging jet. They obtained the streamwise flow velocity from potential theory and solved the boundary layer and energy equations by a finite difference method to evaluate the flow and the heat-transfer parameters near the plate. Saad et al. (1977) solved the Navier-Stokes and energy equations to predict the flow and local heat-transfer characteristics of a confined (by an upper plane wall) laminar impinging jet. Mujumdar and Douglas (1980) studied a confined (by an upper plane wall) laminar jet of hot humid air impinging on an isothermal wet surface. They solved simultaneously the flow, mass, and energy equations. No reference to numerical studies about impinging jets confined by a conical wall was found in the literature.

Brief description of the conical cell

The cell is shown in Figure 1. The liquid jet, with an average velocity V_j, enters the cell from a circular nozzle of diameter D_j. Within the cell the jet is confined by a conical wall, which attached to the nozzle and impinges on a flat round-shaped plate of diameter D_p, placed perpendicularly to the axis of the nozzle. The nozzle-to-plate distance, H, was less than one nozzle diameter, and the exit area height, L (distance between the plane containing the basis of the conical wall and the impingement plate), ranged from 0.1 to 0.3 nozzle diameter.

Flow equations

The flow equations are written below, in the stream function-vorticity formulation. The coordinates are normalized by the nozzle diameter, D_j, the velocity components are normalized by the average jet velocity, V_j, and Re represents the jet Reynolds number:

$$\omega r = \frac{\partial^2 \psi}{\partial z^2} - \frac{1}{r}\frac{\partial \psi}{\partial r} + \frac{\partial^2 \psi}{\partial r^2} \tag{1}$$

$$v_r \frac{\partial \omega}{\partial r} + v_z \frac{\partial \omega}{\partial z} - \omega \frac{v_r}{r} = \frac{1}{Re}\left(\frac{\partial^2 \omega}{\partial r^2} - \frac{\omega}{r^2} + \frac{1}{r}\frac{\partial \omega}{\partial r} + \frac{\partial^2 \omega}{\partial z^2} \right). \tag{2}$$

Equation 1 is a Poisson-type of equation and Eq. 2 is the so-called vorticity transport equation. The dimensionless vorticity ω and stream function ψ are defined as

$$\omega = \frac{\partial v_r}{\partial z} - \frac{\partial v_z}{\partial r} \tag{3}$$

$$v_z = -\frac{1}{r}\frac{\partial \psi}{\partial r}; \qquad v_r = \frac{1}{r}\frac{\partial \psi}{\partial z}. \tag{4}$$

These equations are written with the assumption of laminar and incompressible flow, constant fluid properties, and no buoyancy effects.

Numerical domain and boundary conditions

The elliptical nature of the flow equations requires the specification of the boundary conditions at all sides of the numerical domain. The flow is axisymmetric, therefore only half of the cell is taken for the numerical domain (Figure 2). When the inlet flow is fully developed and laminar, the domain begins at approximately one pipe diameter upstream of the nozzle to account for the impingement effects on the flow at the nozzle exit. When the inlet flow is uniform or a developing laminar flow, the calculation domain begins at the nozzle exit.

Boundary I: Fluid Inlet. The dimensionless velocity profile of a fully developed laminar pipe flow is

$$v_r = 0; \qquad v_z = -2(1-4r^2). \tag{5}$$

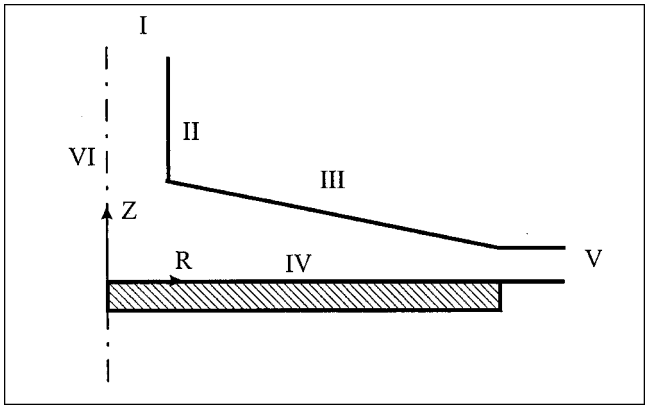

Figure 2. Boundaries of the numerical domain.

For a uniform flow at the nozzle exit, the dimensionless velocity profile is given by

$$v_r = 0; \qquad v_z = -1. \tag{6}$$

A dimensionless developing laminar flow profile can be well approximated by

$$v_r = 0; \qquad v_z = -\frac{n+2}{n}\left[1-(2r)^n\right], \tag{7}$$

where n can take values from 2 (laminar flow) to ∞ (uniform flow).

The stream function and the vorticity function corresponding to the preceding three inlet velocity profiles (Eqs. 5 to 7) can be determined by application of their definitions (Eqs. 3 and 4) using the reference, $\psi = 0$ for $r = 0$ and any z.

- For fully developed laminar flow:

$$\psi = r^2(1-2r^2); \qquad \omega = -16r. \tag{8}$$

- For uniform flow at the nozzle exit:

$$\psi = \frac{r^2}{2}; \qquad \omega = 0. \tag{9}$$

- For a developing laminar flow at the nozzle exit:

$$\psi = \frac{n+2}{n}\left[\frac{1}{2} - \frac{(2r)^n}{n+2}\right]r^2; \qquad \omega = -(n+2)2^n r^{n-1}. \tag{10}$$

Along the solid boundaries (tube wall, conical wall, and impingement surface) the no-slip condition determines the values of the velocity components, as per the following.

Boundary II: Tube Wall.

$$v_z = 0; \qquad v_r = 0; \qquad \psi = \frac{1}{8}; \qquad \omega = -\frac{\partial v_z}{\partial r}. \tag{11}$$

Boundary III: Confining Conical Wall.

$$v_r = 0; \qquad v_z = 0; \qquad \psi = \frac{1}{8}; \qquad \omega = \frac{\partial v_r}{\partial z} - \frac{\partial v_z}{\partial r}. \tag{12}$$

Boundary IV: Impingement Surface.

$$v_r = 0; \qquad v_z = 0; \qquad \psi = 0; \qquad \omega = \frac{\partial v_r}{\partial z}. \tag{13}$$

Boundary V: Fluid Exit. The outlet is located sufficiently far from the zone of interest to allow the application of a condition of developed flow parallel to the impingement plate, which has no upstream influence. Thus,

$$v_z = 0; \qquad \frac{\partial \psi}{\partial r} = 0; \qquad \frac{\partial \omega}{\partial r} = -\frac{\omega}{r}. \tag{14}$$

Boundary VI: Cell Axis. At the axis of symmetry ($r = 0$) the magnitude of the gradients $\partial v_r/\partial z$, $\partial v_z/\partial r$ and $\partial \psi/\partial z$ is null,

$$\psi = 0; \qquad \omega = 0. \tag{15}$$

Numerical method and grid

A finite difference technique was used to discretize the flow equations. The domain is not rectangular, and it was necessary to use a boundary fitted grid. The grid used is shown in Figure 3 and has three distinct zones. In zones A and C the grid is orthogonal and aligned with the jet axis and the impingement plate, thus defining a cylindrical grid. In zone B the grid is still axisymmetric but nonorthogonal; the grid was generated by lines aligned with the jet axis and by inclined lines with different slopes from the conical wall to the impingement plate. These nonorthogonal coordinates are not coincident with the cylindrical coordinates of the equations to be solved, thus an adequate algebraic transformation must be carried out.

The coordinates of the nonorthogonal grid are (s, z) (Figure 4a) with the direction of the unit vector s changing from the direction of the conical wall to that of the impingement plate. The radial coordinate, r, is related with s through the following relation

$$s = \frac{r}{\cos\theta}, \tag{16}$$

with θ ranging from 12° (inclination of the conical wall) to 0^0 (inclination of the impingement plate).

The flow equations were transformed from cylindrical into grid coordinates by using the preceding transformation

$$\omega r = \left(1+tg^2\theta\right)\left(\frac{\partial^2\psi}{\partial z^2} + \frac{\partial^2\psi}{\partial s^2}\right) - \frac{1}{r\cos\theta}\frac{\partial\psi}{\partial s} - \frac{tg\theta}{r}\frac{\partial\psi}{\partial z} + \frac{2tg\theta}{\cos\theta}\frac{\partial^2\psi}{\partial z\partial s} \tag{17}$$

$$v_r\frac{1}{\cos\theta}\frac{\partial\omega}{\partial s} + \left(v_z + tg\theta\, v_r\right)\frac{\partial\omega}{\partial z} - \frac{v_r}{r}\omega = \frac{1}{Re}\left[\left(1+tg^2\theta\right)\left(\frac{\partial^2\omega}{\partial z^2} + \frac{\partial^2\omega}{\partial s^2}\right) + \frac{2tg\theta}{\cos\theta}\frac{\partial^2\omega}{\partial z\partial s} + \frac{1}{r\cos\theta}\frac{\partial\omega}{\partial s} + \frac{tg\theta}{r}\frac{\partial\omega}{\partial z} - \frac{\omega}{r^2}\right], \tag{18}$$

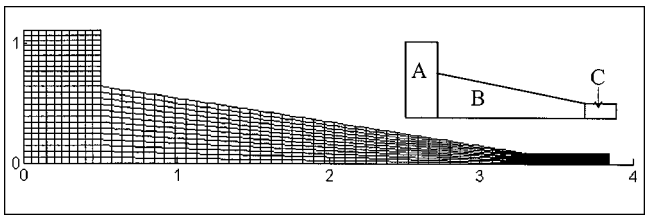

Figure 3. Representation of the grid employed in the numerical study.

In regions A and B + C, the grid had (21 × 97) and (100 × 53) nodes in the r- and z-directions, respectively.

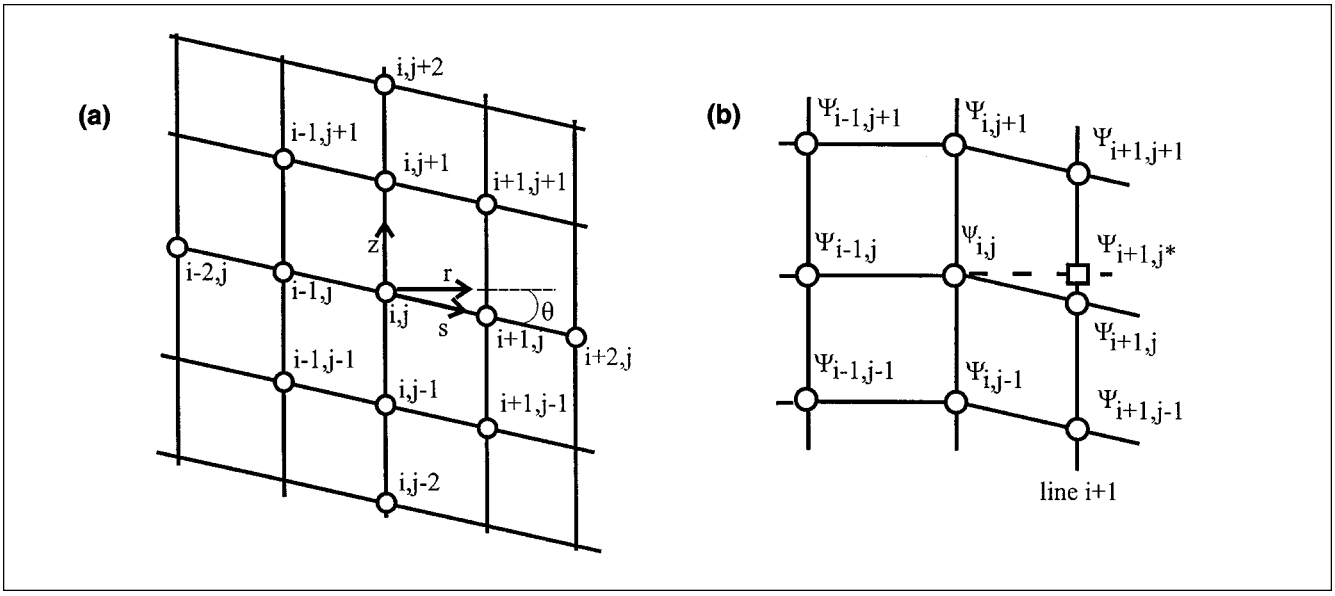

Figure 4. Representation of the grid in the nonorthogonal region.

(a) Coordinates of the grid and detail around the node (i, j); (b) illustration of the interpolation scheme applied to the nodes connecting zones A–B.

with

$$v_z = -\frac{1}{r}\left(\frac{1}{\cos\theta}\frac{\partial\psi}{\partial s} + tg\theta\frac{\partial\psi}{\partial z}\right); \qquad v_r = \frac{1}{r}\frac{\partial\psi}{\partial z}. \quad (19)$$

Equations 17–19 apply everywhere in the domain, even in zones A and C where $\theta = 0$.

The first and second derivatives in Eqs. 17–19 were discretized in the internal nodes of the domain. In the Poisson equation, the derivatives were approximated by a second-order accurate central difference scheme. After discretization an equation of the form

$$\omega_{i,j}r_{i,j} = A_1\psi_{i-1,j} + A_2\psi_{i+1,j} + A_3\psi_{i,j} + A_4\psi_{i,j-1} + A_5\psi_{i,j+1} + A_6\psi_{i-1,j-1} + A_7\psi_{i+1,j-1} + A_8\psi_{i-1,j+1} + A_9\psi_{i+1,j+1} \quad (20)$$

was obtained for each node, where the coefficients A_1 to A_9 are listed in the Appendix.

For the nodes connecting zones A–B and B–C, the second-order central-difference scheme is applicable only with the help of auxiliary nodes located out of the grid, because there is a discontinuity in direction s. For the nodes connecting zones A–B, the discretized Poisson equation is of the form

$$\omega_{i,j}r_{i,j} = A_1\psi_{i-1,j} + A_2\psi_{i+1,j^*} + A_3\psi_{i,j} + A_4\psi_{i,j-1} + A_5\psi_{i,j+1} \quad (21)$$

where ψ_{i+1,j^*} is the value of the stream-function variable at the auxiliary node, represented in Figure 4b by a square symbol. The value of ψ_{i+1,j^*} was obtained through a fourth-order polynomial interpolation applied to the values in the four nearest nodes to $(i+1,\ j^*)$ located in the vertical line $(i+1)$ of the nonorthogonal grid. The coefficients A_1 to A_5 are listed in the Appendix. An identical procedure was applied to the nodes connecting zones B–C.

At the boundaries, the radial coordinate was transformed into the nonorthogonal coordinate with Eq. 16, and the derivatives were approximated by forward or backward difference, with an accuracy of second order, always in the inward cell direction. For the stream-function boundary conditions, an equation of the form

$$B_1\psi_{i-2,j} + B_2\psi_{i-\lambda,j} + B_3\psi_{i,j} = b \quad (22)$$

was obtained for each node, where the coefficients B_1 to B_3 and b are listed in the Appendix.

The vorticity transport equation was discretized by an upwind scheme: the derivatives of the diffusive terms were approximated by central difference and the derivatives of the convective terms by forward or backward difference; in both approximations the accuracy was of second order. For the nodes next to the boundaries, the first derivatives of the convective terms were approximated by forward or backward difference, with an accuracy of first order. For each node an equation of the form

$$C_1\omega_{i-1,j} + C_2\omega_{i+1,j} + C_3\omega_{i,j} + C_4\omega_{i,j-1} + C_5\omega_{i,j+1} + C_6\omega_{i-1,j-1} + C_7\omega_{i+1,j-1} + C_8\omega_{i-1,j+1} + C_9\omega_{i+1,j+1} + C_{10}\omega_{i-2,j} + C_{11}\omega_{i+2,j} + C_{12}\omega_{i,j-2} + C_{13}\omega_{i,j+2} = 0 \quad (23)$$

was obtained, where the coefficients C_1 to C_{13} are listed in the Appendix.

For the nodes connecting zones A–B and B–C the interpolation method described for the Poisson equation was applied. The vorticity transport equation was discretized in these

nodes by an upwind scheme of first order: the derivatives of the diffusive terms were discretized by a second-order accurate central difference scheme, and the derivatives of the convective terms by a first-order accurate forward or backward difference scheme.

The vorticity boundary conditions were discretized by applying an identical scheme to that described earlier for the stream-function boundary conditions, and an equation of the form

$$R_{i,j} = \frac{A_1\psi_{i-1,j} + A_2\psi_{i+1,j} + A_3\psi_{i,j} + A_4\psi_{i,j-1} + A_5\psi_{i,j+1} + A_6\psi_{i-1,j-1} + A_7\psi_{i+1,j-1} + A_8\psi_{i-1,j+1} + A_9\psi_{i+1,j+1} - \omega_{i,j}r_{i,j}}{A_3\psi_{i,j}},$$

$$D_1\omega_{i-2,j} + D_2\omega_{i-1,j} + D_3\omega_{i,j} = d \qquad (24)$$

was obtained for each node where the coefficients D_1 to D_3 and d are listed in the Appendix.

After discretization, two sets of interrelated algebraic equations were obtained. One set arises from the discretization of the Poisson equation and stream-function boundary conditions, the other set from the discretization of the vorticity transport equation and vorticity boundary conditions. They were solved by an iterative procedure and in each step the first set was solved by the alternating direction implicit (ADI) method and the second set by the Gauss-Seidel method.

The convergence of the iterative procedure was studied following the evolution of the values of v_r. This study requires the prior identification of the region with the slowest convergence rate, usually at the beginning of the expansion region, followed by the choice of a representative point. The iterative evolution of the values of v_r in such a location was carried out and is plotted in Figure 5 for $Re = 300$. The values of v_r converge asymptotically to a constant value (v_r^∞). After the 1000th iteration the absolute difference $|v_r^\infty - v_r^{1000\text{th}}|$ is less than 10^{-3},and the absolute difference between consecutive values is always less than 10^{-5}. Similar conclusions were obtained regardless of the jet Reynolds number.

The convergence of the iterative procedure was also studied following the evolution of the sum of the total normalized residues. For example, for the vorticity transport equation,

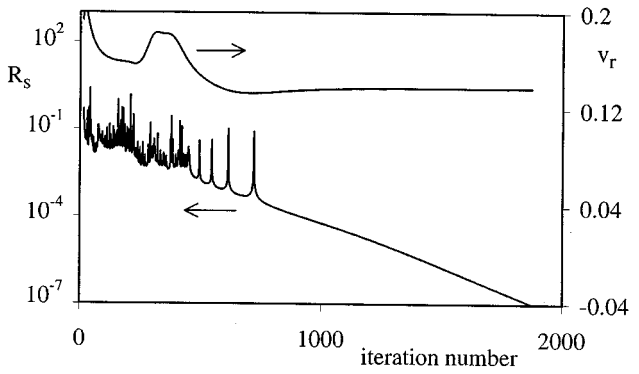

Figure 5. Analysis of the convergence of the iterative process.

Evolution of v_r and of R_s along the iterations at $Re = 300$.

the total normalized residue was defined by

$$R_{(20)} = \frac{\sum_{i=1}^{m}\sum_{j=1}^{n_i}|R_{i,j}|}{p}, \qquad (25)$$

with

where p is the number of the internal nodes of the grid.

The sum of the total residues, represented by R_s, is the sum of $R_{(20)}$ with the residual of Eq. 23 and of all boundary conditions, that is,

$$R_s = R_{(20)} + R_{(22)} + R_{(23)} + R_{(24)}. \qquad (26)$$

The iterative evolution of R_s is also represented in Figure 5 for $Re = 300$. There is a decrease in the value of R_s along the computation, and after about 1000 iterations its value is 5×10^{-5}, three to four orders of magnitude less than at the beginning of the process. Similar conclusions were obtained regardless of the jet Reynolds number.

The fact that, after 1,000 iterations the values of v_r tends toward a stabilized value with R_s still decreasing, confirms the convergence of the iterative method to correct values.

A criterion of convergence was established: the iterative process was completed when during one hundred iterations the absolute difference between consecutive values of v_r was less than 10^{-5} and the value of R_s was also less than 10^{-5}.

The accuracy of the numerical method was determined from solutions on successively refined grids. The rms error defined by Fletcher (1988), and based on the normalized velocity components, was used for that purpose:

$$\text{rms}(v_r) = \left[\left(\sum_{i=1}^{m}\sum_{j=1}^{n_i}\left(v_{r_{i,j}}^* - v_{r_{i,j}}\right)^2\right)/p\right]^{1/2}, \qquad (27)$$

where starred and non-starred values represent quantities calculated with grids having p^* and p number of nodes, respectively.

Three tests were performed to study the solution accuracy. The grids used, and the values of rms found are shown in Table 1. The values of v_r and v_z taken for reference were those obtained with the finest grid. The schemes used in the

Table 1. Results of the Accuracy Tests at $Re = 685$

Grid Nodes				rms (Eq. 27)	
Zone A		Zone B+C			
r	z	r	z	v_r	v_z
6	25	25	14	0.15	0.044
11	49	50	27	0.034	0.011
21	97	100	53	0.0059	0.0026
41	193	200	105	Reference	Reference

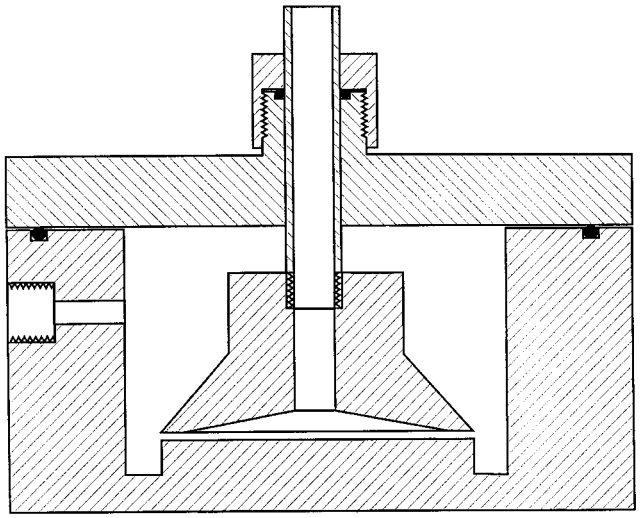

Figure 6. Acrylic test section employed in the laser experiments.

discretization of the equations were of second order in almost all the domain and so, when the grid spacing is halved, the new value of rms is expected to be about 4 times lower than the previous one. The ratios between consecutive rms values in the table are of this order of magnitude, and so it is reasonable to infer that the solution of the algebraic equations is converging to the exact solution. The grid chosen to solve the equations was that in the third line of the table and the respective solutions at $Re = 685$ have an rms error lower than 0.01. This value increases with jet Reynolds number, and is about 0.02 at $Re = 1{,}685$.

Experimental Studies

Test section

Figure 6 shows the acrylic test section. The enclosing box had flat external and internal walls to attenuate the refraction of the laser beams. The internal diameter of the approaching pipe was 11.7 mm and its length was sufficient to guarantee a well-developed velocity profile at the nozzle exit. The pipe and conical wall could be displaced to change the exit area height (L) in the range 1.1 to 3.3 mm. The nozzle-to-plate distance, H, ranged from 7.6 mm to 9.6 mm and the diameter of the impingement plate was $D_p = 77.1$ mm.

The fluids employed were tap water and aqueous solutions of glycerol, and they circulated in a closed circuit at a controlled temperature of 25°C. The density and dynamic viscosity of the water and glycerol solutions at this temperature were measured. The flow rate was adjusted by a control valve and measured by a rotameter.

LDA measurements

The velocity field inside the conical wall was not measured because the refraction of the laser beams did not allow a control volume to be formed. To overcome this difficulty, a liquid with a refractive index matched to that of the acrylic must be used, but for the present purpose it was sufficient to measure the mean radial velocity and the radial turbulence intensity in the cell aperture L, with no curved surface to be crossed by the laser beams.

A 100-mW argon-ion laser was used and the LDA operated in the dual-beam forward-scatter mode. The flow direction was discriminated by an optical frequency shifting of 0.5 or 0.7 MHz from a Bragg cell. The front lens had a focal length of 160 mm, and the half-angle between the two focused beams was 6.45°. The measuring volume dimensions were 0.86 mm in the longitudinal direction of the beams (X) and of 0.10 mm in the two transverse directions, Y and Z (see Figure 7 for the definition of the coordinate system).

The scattering particles were natural contaminants of the fluid and the scattered light was collected by a 300-mm lens and focused on to the pinhole of a photomultiplier before which was placed an interference filter of 514.5 nm. The photomultiplier signal was band-pass filtered to remove high- and low-frequency noise, and the resulting signal was processed by a TSI 1990C counter operating in the single-measurement-per-burst mode, with a frequency validation setting at 1% with 10/16 cycle comparison. The counter was interfaced by a 1400 Dostek card with a 80486-based computer, which provided all the statistical quantities through a purpose-built software.

The test section was placed on an orthogonal coordinate table that allowed displacements in all directions. The displacement uncertainties were ± 0.2 mm in the X- and Y-directions and of ± 0.01 mm in the Z-direction.

The test section was aligned with the laser beams so that (1) the plane containing the laser beams was parallel to the impingement plate; (2) the bisectrix of the angle defined by the laser beams was perpendicular to a lateral wall of the test section; (3) the direction of the bisectrix was coincident with one of the orthogonal coordinates (X in Figure 7). With this alignment, the velocity component in the direction perpendicular to the bisectrix (Y in Figure 7) was measured, that is, the radial velocity component according to Figure 7.

Seven transverse profiles of the radial-velocity component were measured to investigate the flow development. For each profile, the radial velocity was measured at several points along the cell aperture L, the minimum distance between two consecutive measurements being 0.05 mm.

The displacements along Y were done, taking point B as a reference (Figure 7). This point was visually defined as the

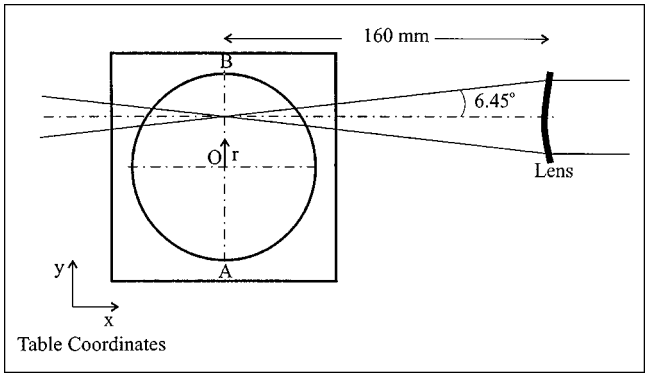

Figure 7. Laser system.

interception of the laser beams with the periphery of the plate; the positioning uncertainty was of the order of magnitude of the displacement error of the test section along Y. For the displacements along Z the reference was the plate surface; the positioning uncertainty was of the order of magnitude of the dimension of the control volume along Z.

Velocity profiles were also measured along the radius OA (Figure 7) to confirm the flow symmetry. The relative deviations between the radial velocity values in axisymmetrical positions were less than 3%.

Flow Patterns

Flow patterns obtained by numerical simulation

The flow inside the cell can be analyzed in three distinct regions: the impingement region, where the flow changes from axial to radial due to the presence of the plate; the wall region, where the radial flow is confined to the downside by the plate and to the upside by the recirculating fluid; and the expansion region, where the fluid is confined by the plate and conical wall. The extension of each region and the corresponding flow patterns depends on geometric (H/D_j, L/D_j, and H/D_p) and hydrodynamic parameters (Re and velocity profile at the nozzle exit). The free jet region upstream of the impingement is not considered here because, as will be shown, the small separation between the plate and the nozzle exit affects the flow, that is, the impingement region starts at the nozzle exit.

Impingement Region. The impingement plate imposes a shift in the jet flow direction. The fluid decelerates in the axial direction, losing kinetic energy that is converted into pressure energy. The deceleration starts at the nozzle exit and intensifies on approaching the plate along the axis. The increased pressure is then transformed into radial momentum of the fluid.

The jet Reynolds number determines the pressure and velocity fields in the impingement region, and can be interpreted as the ratio between the axial inertial flux of momentum and the radial viscous flux of momentum. This interpretation is analogous to that usually found in energy and mass transport, and is adequate to explain the development of the flow. Thus, the kinematic viscosity, ν, becomes the momentum diffusivity by analogy. The entire flow field is three-dimensional and complex; however some details of its development can be emphasized:

1. As soon as the fluid exits the inlet pipe to enter the cell, it ceases to be submitted to the pipe-wall shearing stresses. At low jet Reynolds numbers, the momentum diffusivity enables a fast radial momentum transfer from the center to the periphery of the jet, thus changing the shape of the axial velocity profile and inducing some radial velocity. This transfer process is masked by impingement effects at the nozzle exit region.

2. The internal shearing stresses, which are proportional to the momentum diffusivity, play a shock-absorber role during the axial deceleration of the fluid. At low jet Reynolds numbers, this dampening effect elongates the deceleration zone axially toward the nozzle.

3. In the immediate vicinity of the cell axis and of the plate, the fluid turns radially. This stagnation zone has the highest pressures, and consequently the flow in the vicinity becomes radial with the highest momentum. At low jet Reynolds numbers, the momentum diffusivity quickly spreads this radial momentum axially, and the fluid placed at the periphery of the jet and far from the plate also shifts its flow direction.

In summary, the radial and axial extension of the decelerated zone is largely dependent on the jet Reynolds number value. This is shown well in the streamline plots of Figure 8a at two different values of Re. The lower the jet Reynolds number, the larger the zone of influence of the plate, that is, fluid further away from the wall changes in direction.

The cell region bounded by the conical wall and by the radial flowing fluid is occupied by a recirculating region.

The flow in the impingement region can be modified by geometric or hydrodynamic parameters. In this respect, the numerical simulations showed that:

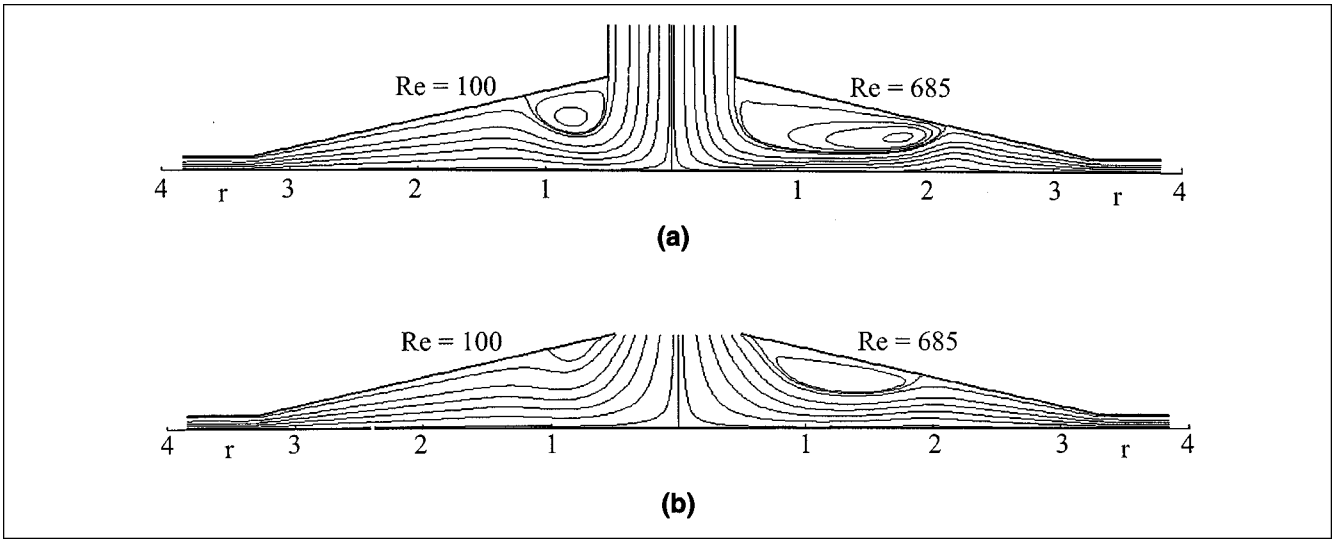

Figure 8. Streamlines representation for $Re = 100$ and for $Re = 685$ at $L/D_j = 0.1$ and different inlet conditions.

(a) Parabolic velocity profile at the nozzle exit; (b) uniform velocity profile at the nozzle exit.

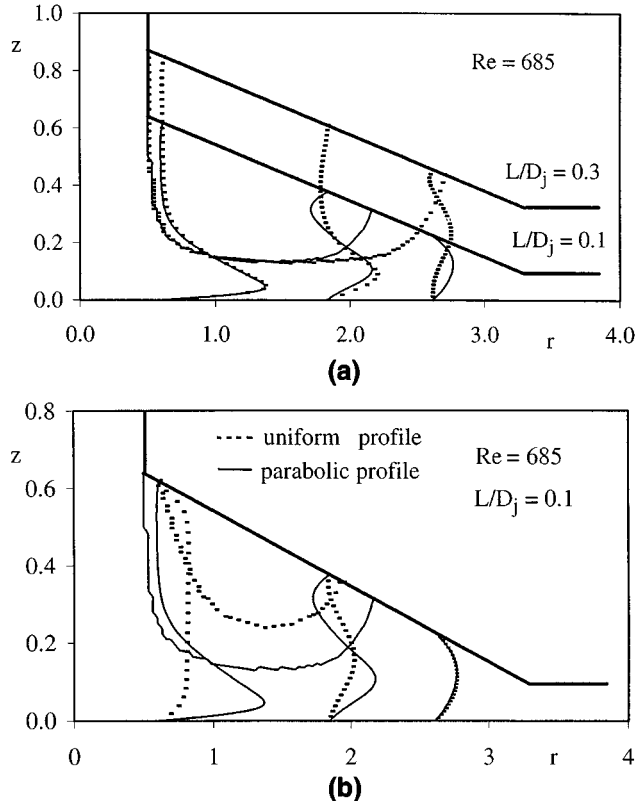

Figure 9. Radial velocity profiles and streamline bordering the first recirculation zone for *Re* = 685.

(a) Parabolic velocity profile at the nozzle exit for $L/D_j = 0.1$ and for $L/D_j = 0.3$; (b) parabolic and uniform velocity profiles at the nozzle exit and $L/D_j = 0.1$.

1. For any jet Reynolds number, a change of the dimensionless distance L/D_j, within the range 0.1 to 0.3, does not affect the flow field; the streamlines for $L/D_j = 0.1$ are identical to those pertaining to $L/D_j = 0.3$. The corresponding radial velocity profiles at the exit of the impingement region are compared in Figure 9a for $Re = 685$, and they are similar.

2. The velocity profile at the nozzle exit determines the flow pattern in the impingement region. The deceleration/acceleration rates of the fluid depend on the initial radial momentum distribution of the jet. If the momentum profile at the nozzle exit is uniform instead of parabolic (for the same bulk velocity), the zone of increased pressure is larger and the fluid in the periphery of the jet shifts direction farther from the plate. In Figure 8b a spread flow and a small recirculation zone are observed.

Wall Region. The predominantly radial flow in the wall region is confined by the impingement plate and the recirculation region. The recirculation length increases radially with the jet Reynolds number, as can be assessed from the streamline plots of Figure 10a corresponding to $L/D_j = 0.1$.

At low jet Reynolds numbers, the low radial velocities at the exit of the impingement region, together with a high-momentum diffusivity, provide conditions for a fast expansion of the fluid to the entire cell cross-section area. In spite of the adverse pressure gradient in the expansion region, no separation was observed for the fluid flowing next to the plate.

With increasing jet Reynolds numbers, the high radial velocity in the thin layer next to the impingement plate and the low local momentum diffusivity delay the expansion of the fluid.

When L/D_j increases, the thickness of this fluid layer remains practically unchanged, and there is a small extension of the recirculation zone in the radial direction. The radial velocity profiles at the inlet, middle, and outlet of the wall region and the streamline bordering the recirculation regions are represented in Figure 9a for $Re = 685$ and two values of L/D_j (0.1 and 0.3). At the inlet and middle of the wall region, the radial velocity profiles coincide, but they are not comparable at the exit due to the difference in cell geometry. The inlet velocity profile has a sharp shape, with the highest velocity near the plate. Along the wall region, the boundary layer develops and the maximum radial velocity moves away from the plate.

The velocity profile at the nozzle exit has a large influence on the flow in the impingement region and consequently along the wall region. Figure 9b compares the radial velocity profiles at the inlet, middle, and outlet of the wall region and the shape of the recirculation zones for the uniform and parabolic profiles at the nozzle exit at $Re = 685$. For a uni-

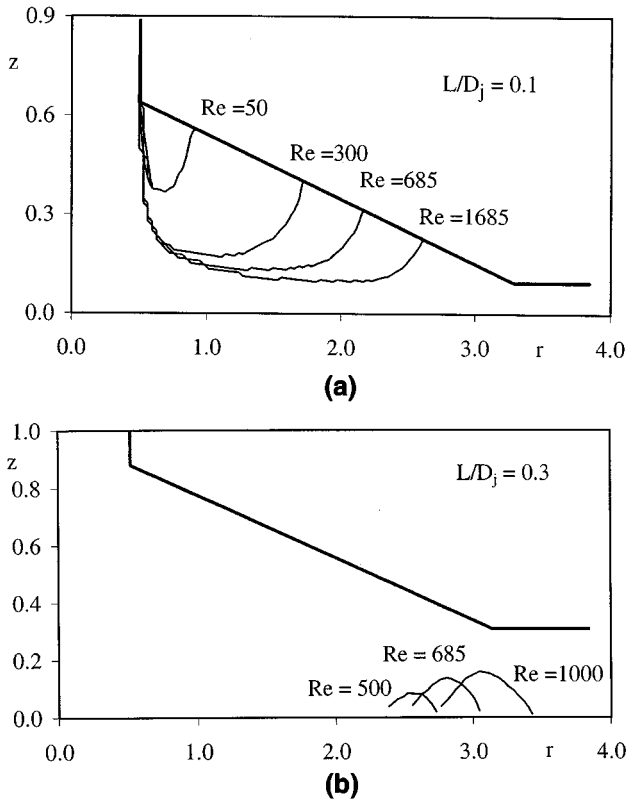

Figure 10. Streamlines bordering the recirculation zones for parabolic velocity profile at the nozzle exit.

(a) First recirculation zone for different *Re* at $L/D_j = 0.1$; (b) second recirculation zone for different *Re* at $L/D_j = 0.3$.

form-velocity inlet, the recirculation zone is shorter, the channel along the wall region is thicker, and the fluid has a lower velocity than for the parabolic inlet.

Expansion Region. The expanding flow downstream of the recirculation depends on the jet Reynolds number as follows:

1. For low jet Reynolds numbers, if the radial-flow cross-section area increases with r (for the present case, the maximum area normal to the flow is reached at $r = 1.7$ for $L/D_j = 0.1$), the fluid flows against an adverse pressure field with loss of momentum, but no fluid separation from the plate occurs.

2. When increasing jet Reynolds numbers, a second recirculation zone develops close to the impingement plate. Fluid flows radially along the wall region against an adverse pressure gradient, and hence with a constant loss of momentum. By the time the cross-section area increases at the end of the first recirculation zone, the remaining momentum is not enough to prevent fluid separation from the plate. The extension and location of this second recirculation zone depends on *Re*, L/D_j, and the velocity profile at the nozzle exit.

As stated earlier, for increasing values of L/D_j, there is a slight extension of the upper recirculation zone, as shown in Figure 9a. In spite of this extension, the cross-section area increases and the fluid expansion occurs in a more adverse pressure field. This results in an enlargement of the second recirculation zone; the corresponding limiting streamlines for $L/D_j = 0.3$ and several values of *Re* are represented in Figure 10b. For $Re = 1000$, the recirculation zone is located close to the exit of the cell, and for increasing values, the recirculation zone exits the cell, originating an inflow of liquid and promoting instability.

For any jet Reynolds number and in the investigated range of L/D_j, when the profile at the nozzle exit is uniform, the second recirculation zone is not observed. The momentum lost by the flow along the wall region is not enough to induce separation during fluid expansion.

For low jet Reynolds numbers, regardless of what the velocity profiles at the nozzle exit are, the radial velocity profiles coincide after the expansion (Figure 9b).

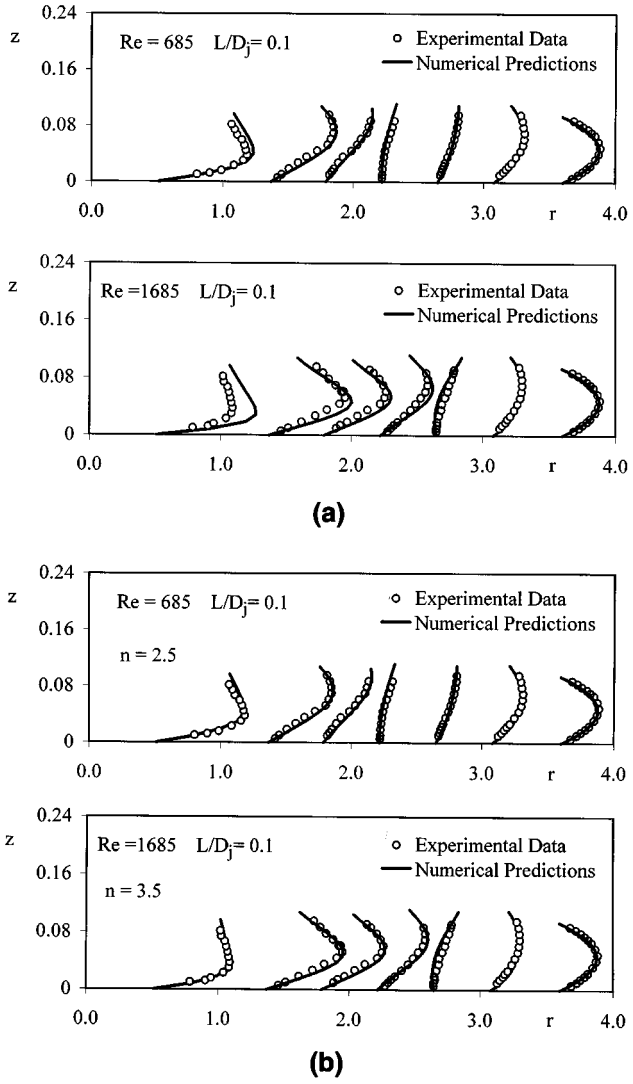

Figure 11. Transverse profiles of the radial velocity component.

Comparison between experimental data and numerical predictions, considering (a) a fully developed laminar profile at the nozzle exit; (b) a developing laminar profile at the nozzle exit, $n = 2.5$ for $Re = 685$ and $n = 3.5$ for $Re = 1685$ (n is the exponent of Eq. 7).

Experimental data

Velocity Profiles. The experimental work had two main objectives: (1) to study the conditions for laminar-to-turbulent transition; and (2) the validation of the simulation data.

These were carried out by measuring the radial velocity profiles of the flow in the aperture L near the impingement surface, where the laser beams did not cross any curved surface. In Figure 11a, the experimental velocity profiles are compared with the numerical predictions for two values of *Re* and the agreement is quite good, except for profiles in the vicinity of the impingement region. Some numerical simulations were carried out to assess the effect of the shape of the inlet velocity profile, and in particular for profiles pertaining to non fully developed flow (different values of n in Eq. 7); it was observed that a small deviation from a fully developed profile was enough to justify that disagreement. This is clearly shown in Figure 11b, which compares experimental data with predictions, taking $n = 2.5$ for $Re = 685$ and $n = 3.5$ for $Re = 1{,}685$; the agreement along the whole plate is now quite good. Since the length of the inlet pipe is theoretically enough to establish a fully developed profile, the presence of small perturbations to the flow in the pipe may be a possible reason for having an undeveloped velocity profile at the inlet.

The profiles of Figure 11a are representative of the numerous profiles obtained for different *Re* and L/D_j.

Laminar-to-Turbulent Transition. In their review article, Polat et al. (1989) observe that for short nozzle-to-impingement plate distances, the flow field is considered laminar up to $Re = 2{,}500$, but they also point out that this value has not been experimentally confirmed.

In order to investigate the conditions for the onset of transition, the mean and fluctuating radial velocity components were measured by LDA, the latter quantified by the statistic rms:

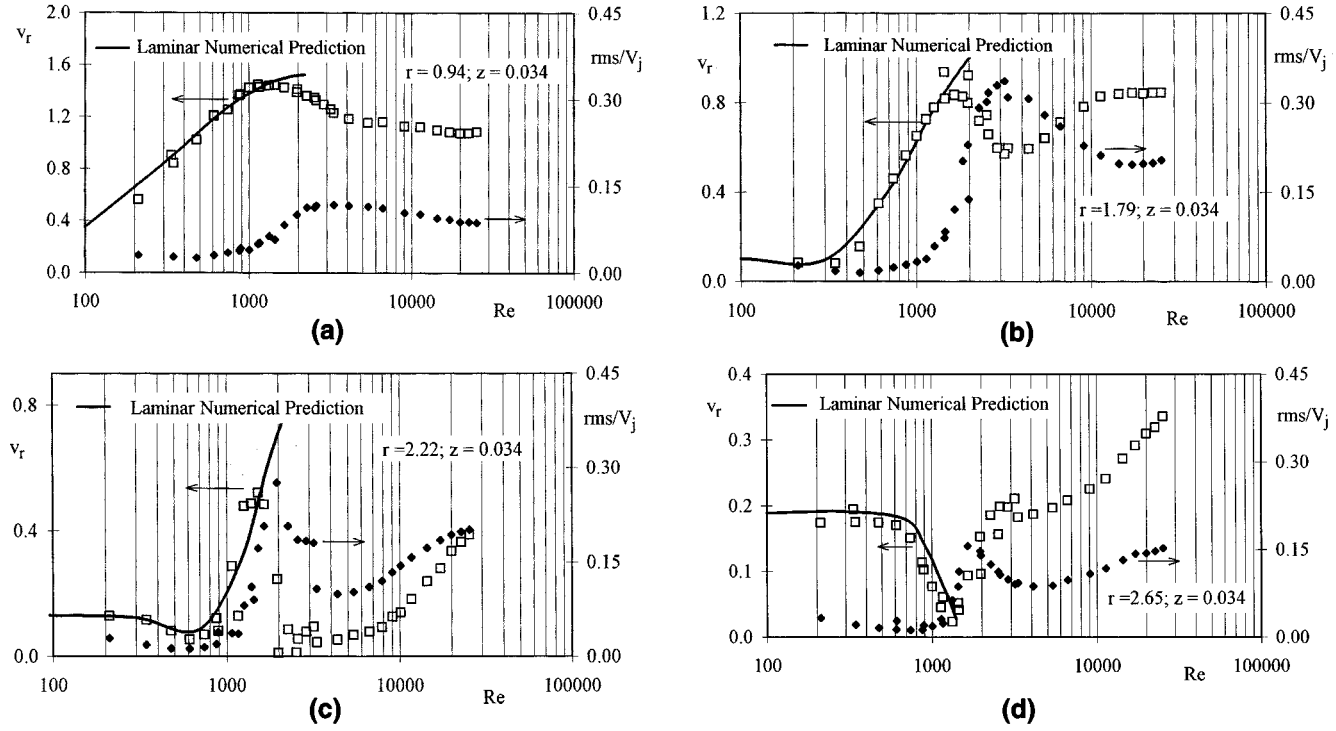

Figure 12. Representation of v_r and of rms/V_j vs. Re at $L/D_j = 0.1$.

The symbols represent laser data and the solid lines numerical laminar predictions: (a) $r = 0.94$ and $z = 0.034$; (b) $r = 1.79$ and $z = 0.034$; (c) $r = 2.22$ and $z = 0.034$; (d) $r = 2.65$ and $z = 0.034$.

$$\text{rms} = \left[\sum_{i=1}^{N} \frac{(v_r)_i - (\overline{v_r})^2}{N-1} \right]^{1/2}, \qquad (28)$$

where $(v_r)_i$ is the ith-instantaneous radial-velocity reading; $\overline{v_r}$ is the mean radial-velocity; and N is the number of data points in the sample ($N > 4{,}000$).

For each jet Reynolds number in the range $100 < Re < 30{,}000$, the measurements were performed in eight radial positions along the flow for the same axial coordinate.

The experimental values of the radial velocity were compared with the corresponding predictions in laminar flow. The agreement was good for the laminar regime, but otherwise a persistent deviation showed the onset of transition. The onset of transition is also marked by a sudden increase in the rms values. This comparison is carried out in Figures 12a–12d, which are representative of the $L/D_j = 0.1$ case. In each figure part, v_r and rms/V_j are plotted against Re for each radial position in a semilog scale.

For Re above 200, the data represented in Figures 12a and 12b were obtained in the wall region, in positions below the recirculation zone. A good agreement is observed at low jet Reynolds numbers, but above a critical value there is a persistent deviation when comparing experimental and numerical mean-velocity values. This critical jet Reynolds number is approximately the same at which rms/V_j starts to increase. In Figure 12a such critical Re is around 1,400, while in Figure 12b it is around 1,600.

For Re above 600, the data represented in Figure 12c were obtained below the recirculation zone. The mean and the fluctuating velocities vary in the same way as previously, with the experimental values of v_r beginning to deviate from the predictions when the rms/V_j values start to increase at an Re around 1,600.

The data of Figure 12d were measured in the region where the second recirculation zone develops. The experimental values of v_r begin to deviate from the predictions at an Re around 1,600, whereas the rms/V_j starts to increase earlier, at an Re around 1,400.

In conclusion, the majority of the experimental data suggest that the laminar–turbulent transition occurs at around $Re = 1{,}600$. Similar values of critical Re observed along different radial positions suggest that transition probably begins at the impingement region.

An identical study was carried out for $L/D_j = 0.3$ and the same conclusions were drawn.

Flow confined by: conical wall vs. parallel plate

The flow patterns inside a cell with a plate attached to the nozzle and parallel to the impingement surface were obtained by numerical simulation. That flow pattern is presented in Figure 13 and compared with that obtained in a conical cell, for $Re = 400$ and with the same nozzle-to-impingement-plate distance. The flow patterns are similar, except that with the parallel-plate confinement both recirculation zones are longer. When the confinement plates are short, the recirculating zones burst through the outflow boundary, leading to an inflow that promotes instability inside the cell. For the geometry studied ($D_p/D_j = 6.6$, $H/D_j = 0.65$) this recirculation zone bursts at an $Re \approx 400$.

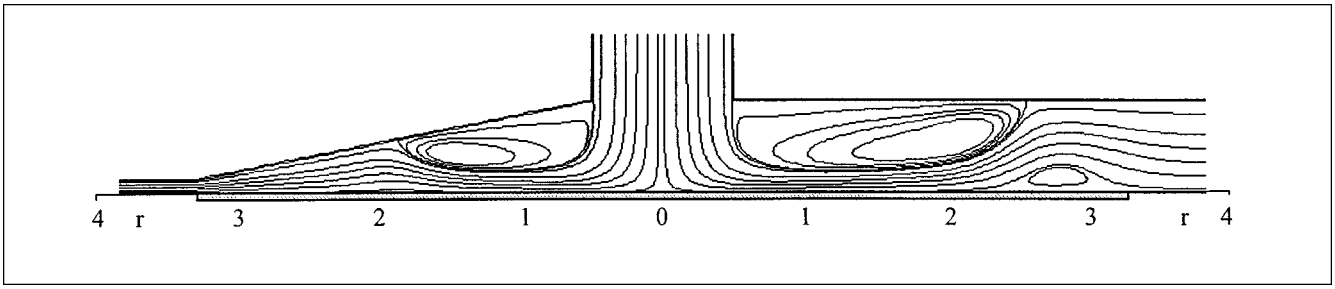

Figure 13. Flow pattern developed in a conical cell vs. a cell with parallel plates at $Re = 400$ and $H/D_j = 0.65$.

Conclusions

The laminar flow of a jet confined by a conical wall extending from the nozzle to a short distance above an impingement plate can be analyzed separately in three regions: the impingement region, the wall region, and the expansion region. The jet Reynolds number and the inlet velocity profile have a strong influence on the whole flow, while the nozzle-to-plate distance is influential only in the expansion region. At low jet Reynolds numbers, the fluid far from the plate acquires radial velocity and a short recirculation zone close to the conical wall is observed. At high jet Reynolds numbers, this recirculating zone enlarges, the fluid flows radially in a thin channel attached to the impingement plate, and a second recirculation zone develops in the expansion region, close to the plate. If the nozzle-to-plate distance increases, the second recirculation zone enlarges. For the uniform velocity profile at the nozzle exit, instead of parabolic, the fluid flows in a thick channel with a low radial velocity, and the second recirculation zone does not develop. Transition from laminar to turbulent flow probably begins in the impingement region at an *Re* around 1600. The effect of the conical confinement on the flow is felt in the size of the recirculation zones: for the same jet Reynolds number the recirculation zones are longer when the confinement is accomplished by parallel plates. Then, for small impinging plates, the conical wall has a stabilizing effect on the flow, preventing the recirculation zones from bursting through the exit of the cell.

Acknowledgments

The authors acknowledge the financial support given by JNICT, project PBIC/C/CEN/1337/92, and by F.C.T., Project PRAXIS/C/EQU/12141/1998.

Notation

m = number of nodes of the grid along boundary IV
n_i = number of nodes along the ith verical line of the grid
r = dimensionless radial coordinate, R/D_j
R = radial coordinate, m
v_r = dimensionless radial velocity, V_r/V_j
v_z = dimensionless axial velocity, V_z/V_j
V_r = radial velocity, $m \cdot s^{-1}$
V_z = axial velocity, $m \cdot s^{-1}$
z = dimensionless axial coordinate, Z/D_j
Z = axial coordinate, m

Literature Cited

Fletcher, C. A. J., *Computational Techniques for Fluid Dynamics I, Springer Series in Computational Physics*, Springer-Verlag, Berlin (1988).

Gardon, R., and J. C. Akfirat, "The Role of Turbulence in Determining the Heat Transfer Characteristics of Impinging Jets," *Int. J. Heat Mass Transfer*, **8**, 1261 (1965).

Garimella, S. V., and R. A. Rice, "Confined and Submerged Liquid Jet Impingement Heat Transfer," *ASME J. Heat Transfer*, **117**, 871 (1995).

Martin, H., "Heat and Mass Transfer Between Impinging Gas Jets and Solid Surfaces," *Adv. Heat Transfer*, **13**, 1 (1977).

Miyazaki, H., and E. Silberman, "Flow and Heat Transfer on a Flat Plate Normal to a Two-Dimensional Laminar Jet Issuing from a Nozzle of Finite Height," *Int. J. Heat Mass Transfer*, **15**, 2097 (1972).

Mujumdar, A. S., Y. K. Li, and W. J. M. Douglas, "Evaporation Under an Impinging Jet: A Numerical Model," *Can. J. Chem. Eng.*, **58**, 448 (1980).

Polat, S., B. Huang, A. S. Mujumdar, and W. J. M. Douglas, "Numerical Flow and Heat Transfer Under Impinging Jets: A Review," *Ann. Rev. Numer. Fluid Mech. Heat Transfer*, **2**, 157 (1989).

Saad, N. R., W. J. M. Douglas, and A. S. Mujumdar, "Prediction of Heat Transfer Under an Axi-Symmetric Laminar Impinging Jet," *Ind. Eng. Chem., Fundam.*, **16**, 148 (1977).

Appendix

The coefficients of the discretized flow equations, presented in this Appendix, are expressed for the node (i, j) represented in Figure 4a.

The coefficients of the discretized Poisson equation are computed from the following expressions:

$$A_1 = A_{1,1} + A_{1,2} + A_{1,3} \qquad A_2 = \delta_j A_{1,1} - \delta_j^2 A_{1,2} - \delta_j^2 A_{1,3}$$

$$A_3 = -\left(A_1 + A_2 + A_{4,1} + A_{4,2} + \epsilon A_{4,1} - \epsilon^2 A_{4,2}\right)$$

$$A_4 = A_{4,1} + A_{4,2} - A_6 - A_7$$

$$A_5 = \epsilon A_{4,1} - \epsilon^2 A_{4,2} - A_8 - A_9$$

$$A_6 = \frac{A_0 (z_{i,j+1} - z_{i,j})^2 (r_{i+1,j-1} - r_{i,j-1})}{(r_{i,j-1} - r_{i-1,j-1})(r_{i+1,j-1} - r_{i-1,j-1})\beta_{j-1}}$$

$$A_7 = -\delta_{j-1}^2 A_6$$

$$A_8 = -\frac{A_0 (z_{i,j} - z_{i,j-1})^2 (r_{i+1,j+1} - r_{i,j+1})}{(r_{i,j+1} - r_{i-1,j+1})(r_{i+1,j+1} - r_{i-1,j+1})\beta_{j+1}}$$

$$A_9 = -\delta_{j+1}^2 A_8,$$

where

$$A_0 = \frac{2\alpha_j \beta_j}{(z_{i,j} - z_{i,j-1})(z_{i,j+1} - z_{i,j})(z_{i,j+1} - z_{i,j-1})}$$

$$A_{1,1} = \frac{2\left(1+\alpha_j^2\right)}{(r_{i,j}-r_{i-1,j})(r_{i+1,j}-r_{i-1,j})\beta_j^2}$$

$$A_{1,2} = \frac{A_0\left[(z_{i,j}-z_{i,j-1})^2-(z_{i,j+1}-z_{i,j})^2\right](r_{i+1,j}-r_{i,j})}{(r_{i,j}-r_{i-1,j})(r_{i+1,j}-r_{i-1,j})\beta_j}$$

$$A_{1,3} = \frac{r_{i+1,j}-r_{i,j}}{r_{i,j}(r_{i,j}-r_{i-1,j})(r_{i+1,j}-r_{i-1,j})}$$

$$A_{4,1} = \frac{2\left(1+\alpha_j^2\right)}{(z_{i,j}-z_{i,j-1})(z_{i,j+1}-z_{i,j-1})}$$

$$A_{4,2} = \frac{\alpha_j(z_{i,j+1}-z_{i,j})}{r_{i,j}(z_{i,j}-z_{i,j-1})(z_{i,j+1}-z_{i,j-1})}$$

and

$$\alpha_j = \frac{z_{i-1,j}-z_{i+1,j}}{r_{i+1,j}-r_{i-1,j}}$$

$$\beta_j = \frac{\sqrt{(z_{i-1,j}-z_{i+1,j})^2+(r_{i+1,j}-r_{i-1,j})^2}}{r_{i+1,j}-r_{i-1,j}}$$

$$\delta_j = \frac{r_{i,j}-r_{i-1,j}}{r_{i+1,j}-r_{i,j}} \qquad \epsilon = \frac{z_{i,j}-z_{i,j-1}}{z_{i,j+1}-z_{i,j}}.$$

The coefficients of the discretized vorticity transport equation are computed from the following expressions:

$$C_1 = C_{1,1}+C_{1,2}+C_{1,3}+C_{1,4}$$

$$C_2 = -\delta_j^2 C_{1,2}+\delta_j C_{1,3}-\delta_j^2 C_{1,4}+C_{2,1}$$

$$C_3 = -\left(C_1+C_2+C_{4,2}+C_{4,3}+C_{5,1}-\epsilon^2 C_{4,2}+\epsilon C_{4,3}+C_{10}+C_{11}+C_{12}+C_{13}\right)+\frac{1}{Re\, r_{i,j}^2}-\frac{v_{r_{i,j}}}{r_{i,j}}$$

$$C_4 = C_{4,1}+C_{4,2}+C_{4,3}-C_6-C_7$$

$$C_5 = -\epsilon^2 C_{4,2}+\epsilon C_{4,3}+C_{5,1}-C_8-C_9$$

$$C_6 = \frac{C_0(z_{i,j+1}-z_{i,j})^2(r_{i+1,j-1}-r_{i,j-1})}{(r_{i,j-1}-r_{i-1,j-1})(r_{i+1,j-1}-r_{i-1,j-1})\beta_{j-1}}$$

$$C_7 = -\delta_{j-1}^2 C_6$$

$$C_8 = -\frac{C_0(z_{i,j}-z_{i,j-1})^2(r_{i+1,j+1}-r_{i,j+1})}{(r_{i,j+1}-r_{i-1,j+1})(r_{i+1,j+1}-r_{i-1,j+1})\beta_{j+1}}$$

$$C_9 = -\delta_{j+1}^2 C_8$$

$$C_{10} = -\frac{C_{1,1}(r_{i,j}-r_{i-1,j})^2}{(r_{i,j}-r_{i-2,j})^2} \qquad C_{11} = -\frac{C_{2,1}(r_{i+1,j}-r_{i,j})^2}{(r_{i+2,j}-r_{i,j})^2}$$

$$C_{12} = -\frac{C_{4,1}(z_{i,j}-z_{i,j-1})^2}{(z_{i,j}-z_{i,j-2})^2} \qquad C_{13} = -\frac{C_{5,1}(z_{i,j+1}-z_{i,j})^2}{(z_{i,j+2}-z_{i,j})^2},$$

where

$$C_0 = -\frac{1}{Re}A_0$$

$$C_{1,1} = \begin{cases} v_{r_{i,j}} > 0 & -\dfrac{v_{r_{i,j}}(r_{i,j}-r_{i-2,j})}{(r_{i,j}-r_{i-1,j})(r_{i-1,j}-r_{i-2,j})} \\ v_{r_{i,j}} < 0 & 0 \end{cases}$$

$$C_{1,2} = \frac{r_{i+1,j}-r_{i,j}}{r_{i,j}(r_{i,j}-r_{i-1,j})(r_{i+1,j}-r_{i-1,j})\beta_j Re}$$

$$C_{1,3} = -\frac{2\left(1+\alpha_j^2\right)}{(r_{i,j}-r_{i-1,j})(r_{i+1,j}-r_{i-1,j})Re\beta_j^2}$$

$$C_{1,4} = \frac{C_0(r_{i+1,j}-r_{i,j})\left[(z_{i,j}-z_{i,j-1})^2-(z_{i,j+1}-z_{i,j})^2\right]}{(r_{i,j}-r_{i-1,j})(r_{i+1,j}-r_{i-1,j})\beta_j}$$

$$C_{2,1} = \begin{cases} v_{r_{i,j}} > 0 & 0 \\ v_{r_{i,j}} < 0 & \dfrac{v_{r_{i,j}}(r_{i+2,j}-r_{i,j})}{(r_{i+1,j}-r_{i,j})(r_{i+2,j}-r_{i+1,j})} \end{cases}$$

$$C_{4,1} = \begin{cases} v_{z_{i,j}}+\alpha_j v_{r_{i,j}} > 0 & -\dfrac{(z_{i,j}-z_{i,j-2})(v_{z_{i,j}}+\alpha_j v_{r_{i,j}})}{(z_{i,j}-z_{i,j-1})(z_{i,j-1}-z_{i,j-2})} \\ v_{z_{i,j}}+\alpha_j v_{r_{i,j}} < 0 & 0 \end{cases}$$

$$C_{4,2} = \frac{\alpha_j(z_{i,j+1}-z_{i,j})}{r_{i,j}(z_{i,j}-z_{i,j-1})(z_{i,j+1}-z_{i,j-1})Re}$$

$$C_{4,3} = -\frac{2\left(1+\alpha_j^2\right)}{(z_{i,j}-z_{i,j-1})(z_{i,j+1}-z_{i,j-1})Re}$$

$$C_{5,1} = \begin{cases} v_{z_{i,j}}+\alpha_j v_{r_{i,j}} > 0 & 0 \\ v_{z_{i,j}}+\alpha_j v_{r_{i,j}} < 0 & \dfrac{(z_{i,j+2}-z_{i,j})(v_{z_{i,j}}+\alpha_j v_{r_{i,j}})}{(z_{i,j+1}-z_{i,j})(z_{i,j+2}-z_{i,j+1})} \end{cases}$$

with A_0, α_j, and β_j previously defined.

For the nodes located next to the boundaries, the first derivatives of the convective terms in the vorticity transport equation were approximated by a first-order scheme, and so some coefficients are expressed in a different way

$$C_{10} = C_{11} = C_{12} = C_{13} = 0.$$

$$C_{1,1} = \begin{cases} v_{r_{i,j}} > 0 & -\dfrac{v_{r_{i,j}}}{r_{i,j}-r_{i-1,j}} \\ v_{r_{i,j}} < 0 & 0 \end{cases}$$

$$C_{2,1} = \begin{cases} v_{r_{i,j}} > 0 & 0 \\ v_{r_{i,j}} < 0 & \dfrac{v_{r_{i,j}}}{r_{i+1,j}-r_{i,j}} \end{cases}$$

$$C_{4,1}=\begin{cases} v_{z_{i,j}}+v_{r_{i,j}}\alpha_j>0 & -\dfrac{v_{z_{i,j}}+v_{r_{i,j}}\alpha_j}{z_{i,j}-z_{i,j-1}} \\ v_{z_{i,j}}+v_{r_{i,j}}\alpha_j<0 & 0 \end{cases}$$

$$C_{5,1}=\begin{cases} v_{z_{i,j}}+v_{r_{i,j}}\alpha_j>0 & 0 \\ v_{z_{i,j}}+v_{r_{i,j}}\alpha_j<0 & \dfrac{v_{z_{i,j}}+v_{r_{i,j}}\alpha_j}{z_{i,j+1}-z_{i,j}} \end{cases}.$$

• The coefficients of the boundary equations are computed from the following expressions:

Boundary I

$$B_1=B_2=0; \qquad B_3=1; \qquad b=\frac{n+2}{n}r_{i,j}^2\left[\frac{1}{2}-\frac{(2r_{i,j})^n}{n+2}\right]$$

$$D_1=D_2=0; \qquad D_3=1; \qquad d=-(n+2)2^n r_{i,j}^{n-1}.$$

Boundary II

$$B_1=B_2=0; \qquad B_3=1; \qquad b=\frac{1}{8}$$

$$D_1=D_2=0; \qquad D_3=1; \qquad d=\frac{4v_{z_{i-1,j}}-v_{z_{i-2,j}}}{2\Delta r_j},$$

with $\Delta r_j=r_{i,j}-r_{i-1,j}=r_{i-1,j}=r_{i-2,j}$.

Boundary III

$$B_1=B_2=0; \qquad B_3=1; \qquad b=\frac{1}{8}$$

$$D_1=D_2=0; \qquad D_3=1;$$

$$d=-\frac{4v_{r_{i,j-1}}-v_{r_{i,j-2}}}{2\Delta z_i}+\frac{z_{i,j}-z_{i+1,j}}{r_{i+1,j}-r_{i,j}}\frac{4v_{z_{i,j-1}}-v_{z_{i,j-2}}}{2\Delta z_i},$$

with $\Delta z_i=z_{i,j}-z_{i,j-1}=z_{i,j-1}-z_{i,j-2}$.

Boundary IV

$$B_1=B_2=0; \qquad B_3=1; \qquad b=0$$

$$D_1=D_2=0; \qquad D_3=1; \qquad d=\frac{4v_{r_{i,j+1}}-v_{r_{i,j+2}}}{2\Delta z_i}$$

with $\Delta z_i=z_{i,j+1}-z_{i,j}=z_{i,j+2}-z_{i,j+1}$.

Boundary V

$$B_1=1; \qquad B_2=-4; \qquad B_3=3; \qquad b=0$$

$$D_1=1; \qquad D_2=-4; \qquad D_3=3+\frac{2\Delta r_j}{r_{i,j}}; \qquad d=0,$$

with $\Delta r_j=r_{i,j}-r_{i-1,j}=r_{i-1,j}-r_{i-2,j}$.

Boundary VI

$$B_1=B_2=0; \qquad B_3=1; \qquad b=0$$

$$D_1=D_2=0; \qquad D_3=1; \qquad d=0.$$

Manuscript received Jan. 28, 1999, and revision received July 27, 1999.